Korean J. Chem. Eng., 40(6), 1353-1359 (2023)
DOI: 10.1007/s11814-022-1370-2

pISSN: 0256-1115
eISSN: 1975-7220

Pseudocapacitive behavior of mesoporous tungsten oxide in aqueous Zn^{2+} electrolyte

Woosuk Kang*, **Inho Nam*,**,†**, **and Changshin Jo***,****,†**

*School of Chemical Engineering & Materials Science, Chung-Ang University (CAU),
84 Heukseok-ro, Dongjak-gu, Seoul 06974, Korea
**Department of Intelligent Energy and Industry, Department of Advanced Materials Engineering,
Chung-Ang University (CAU), 84 Heukseok-ro, Dongjak-gu, Seoul 06974, Korea
***Graduate Institute of Ferrous & Energy Materials Technology (GIFT), Pohang University of Science and Technology
(POSTECH), 77 Cheongam-ro, Nam-gu, Pohang, Gyeongbuk 37673, Korea
****Chemical Engineering, Pohang University of Science and Technology (POSTECH),
77 Cheongam-ro, Nam-gu, Pohang, Gyeongbuk 37673, Korea

(*Received 15 September 2022 • Revised 6 December 2022 • Accepted 8 December 2022*)

Abstract−Aqueous Zn-ion batteries or capacitors have attracted great interest for their potential use in grid-scale energy storage systems (ESSs). They have suitable properties such as high safety, low-cost materials, and stability of Zn^{2+} in aqueous systems. The anode of these systems is mainly based on metallic Zn; however, corrosion of the metal surface and formation of dendrites inhibit their long-term cycle stability. It is thus necessary to find a material that can host Zn^{2+} in a low voltage range and enhance the electrochemical performance. Among various possible strategies, herein we applied nanostructuring to prepare mesoporous WO_3 as anode material and compared the change in the electrochemical performance to that of bulk WO_3. After unveiling the effect of the nanostructure, we conclude that the present nanomaterials show great potential as electrode materials for aqueous Zn-ion systems.

Keywords: Nanomaterials, Mesoporous Metal Oxides, Aqueous Zinc-ion Batteries, Zinc-ion Capacitors, Anode Materials

INTRODUCTION

Owing to their high energy density, Li-ion batteries (LIBs) are mainly used in grid-scale energy storage system (ESSs) that store energy from intermittent sources such as wind, tidal, and solar power. However, the attractiveness of LIBs as candidates for ESSs is compromised by some of their intrinsic problems [1-3]. For example, the enormously increased demand for LIBs has raised the cost of the corresponding materials, and the distribution of resources is also unbalanced, resulting in cost fluctuations. Moreover, the use of flammable organic electrolytes can cause severe safety problems, such as fire hazards and electrolyte leakages, which are followed by side reactions of such electrolytes, resulting in cell failure and even explosions in the worst case. As a result of these problems, aqueous Zn-ion capacitors (ZICs) have attracted increasing attention as alternative energy storage systems, owing to their extremely high earth abundance and high safety [4-6]. Metallic Zn has a high theoretical capacity (~820 mAh g^{-1} and ~5,833 mAh L^{-1}). In addition, the use of aqueous electrolytes eliminates fire hazards and provides environmental friendliness.

Despite these advantages, metallic Zn, mostly used as anode of ZICs, suffers from surface corrosion. This corrosion of metallic Zn results in gas evolution and increased internal resistance of the cell [7]. Moreover, the metal plating process causes uncontrollable metallic Zn formation, resulting in the formation of dendrites and isolated Zn. The Zn dendrites penetrate the separator, leading to short-circuiting and dead Zn formation [8]. Furthermore, the hydrogen evolution reaction (HER) on the metallic Zn surface changes the pH of the electrolyte and increases the internal pressure of the cell [9]. The changed pH conditions can make metallic Zn more corrosive or form byproducts; moreover, the increase in internal pressure can cause swelling of the cell. These problems make the ZIC system unstable during long-term cycling, which inhibits its practical application to systems that require a long lifespan. To overcome these issues, recent studies have proposed the introduction of a protective layer on the metallic Zn surface or the 3D structuring of the metallic Zn. Even though these strategies result in improved performance, side reactions can be accelerated when the new metal surface is exposed during cycling; this issue would require the replacement of the metallic Zn anode with a stable Zn-ion host material.

To realize a stable cell without energy density losses, a new Zn-ion host material is required to have a reaction voltage range similar to the Zn/Zn^{2+} potential (−0.76 V *vs.* standard hydrogen electrode) and a sufficiently high capacity, corresponding to that of the cathode materials. For example, Xiong et al. reported that hexagonal MoO_3 can work as a Zn^{2+}-intercalating anode and shows reversible cycling [10]. Inspired by the MoO_3 anode, it is worth identifying other transition metal-based compounds with similar redox potentials. Therefore, we have conducted preliminary experiments with various metal oxide materials and confirmed that tungsten trioxide (WO_3) undergoes redox reactions in the low-voltage range (0.1-0.9 V *vs.* Zn/Zn^{2+}). As an active material, WO_3 has low cost, high

---

[†] To whom correspondence should be addressed.
E-mail: inhonam@cau.ac.kr, jochangshin@postech.ac.kr

conductivity after ion insertion, high electrochemical stability, and is known to react with Zn-ions in organic electrolytes (0.2 M $Zn(CF_3SO_3)_2$ in 1 : 4 propylene carbonate (PC)-dimethyl sulfoxide (DMSO)) [11-13]. Recently, hexagonal-phase WO_3 has been applied as anode for aqueous Zn-ion batteries (ZIBs) [14]. Combined with 3D porous graphene, hexagonal WO_3 showed promising potential as an alternative to metallic Zn, due to the large size of its channels (diameter=5.36 Å).

To improve the electrochemical performance of active materials, various possible strategies have been applied in the energy storage field, such as conductive layer coating, doping, composite fabrication, and nanostructuring [15-21]. Among various possible methods, in this study we have investigated the effects of nanostructuring on ZIC systems by introducing a 3D-ordered porous structure. The advantages of nanostructuring are as follows: i) nanomaterials have a high specific surface area; because the energy-storage mechanism of capacitors mostly starts from the surface of the active materials *via* adsorption/desorption or redox reactions, the enlarged surface area of the nanomaterials leads to a highly reversible capacitance. Moreover, nanostructuring generates smaller particle sizes with increased near-surface ionic diffusion paths, which leads to a high power performance, owing to the faster redox or intercalation/deintercalation reactions at the surface; ii) the nanostructure can accommodate the volume changes caused by repeated cycles when the ions undergo insertion/extraction in the active material; iii) the nanostructure also provides a short ionic diffusion length, due to the thin pore walls; finally, iv) fast electrolyte penetration can be achieved into the interparticle area or nanosized pores. Nanostructured materials have already been applied in LIBs and showed interesting electrochemical behavior, compared to that of the same material in bulk form. For example, it has been reported that Li^+-intercalating electrode materials, such as nanosized Nb_2O_5, TiO_2, $Li_4Ti_5O_{12}$, and $LiFePO_4$, rapidly react with Li ions, showing a capacitive behavior resulting in high power performance [22-26]. Nanostructured materials are expected to achieve the same results when applied as anodes of ZICs, through an analogous mechanism to that active in LIBs.

Herein, we fabricated mesoporous WO_3 (m-WO_3) with potential application as anode of ZICs. Using a KIT-6 silica template, we successfully prepared a highly ordered m-WO_3 material. To elucidate how the mesoporous structure affects the electrochemical properties, we measured the electrochemical performance of m-WO_3 and compared it with that of bulk WO_3 (b-WO_3), which has the same crystal phase under the same conditions. We carried out galvanostatic charge/discharge (GCD) and cyclic voltammetry (CV) measurements to investigate the electrochemical behavior of each sample, and quantified the contributions of the capacitive or diffusion-controlled reaction mechanisms. m-WO_3 showed more intense redox peaks and different redox potentials, denoting lower polarization (from ~0.3 and ~0.8 V to ~0.45 and ~0.7 V *vs.* Zn/Zn^{2+}, respectively). Furthermore, the contribution of the capacitive reaction was more dominant in the mesoporous structure. We also used *ex situ* X-ray diffraction (XRD) measurements to evaluate the changes in the crystal structure of m-WO_3 and b-WO_3 in each charge/discharge state. We successfully identified the effect of the nanostructure on the phase transition behavior during cycling. These results show that nanostructuring of electrodes can work as an effective strategy to develop improved anodes for ZICs with higher capacitance and longer cycle life.

EXPERIMENTAL SECTION

1. Preparation of KIT-6

The mesoporous silica hard template (KIT-6) was prepared following a previously reported method [27-29]. Six grams of P123 (EO_{20}-PO_{70}-EO_{20}, Sigma Aldrich) and 11.8 g of hydrochloric acid

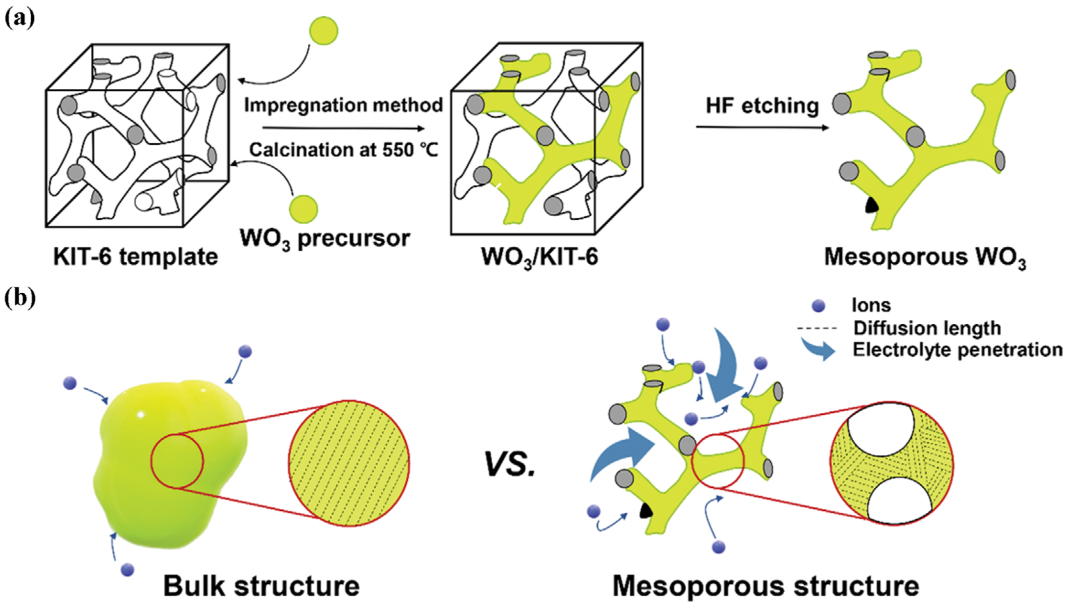

Fig. 1. (a) Synthetic process of m-WO_3 using hard template method. (b) Schematic illustration of effect of mesoporous structure on electrode material.

(Samchun Chemicals) were dissolved in deionized (DI) water and stirred for 6 h at 35 °C. Then, 6 g of butanol (Sigma Aldrich) was added to the solution, which was stirred for another 1 h. Afterward, 12.9 g of tetraethyl orthosilicate (Sigma Aldrich) was added as silica source and stirred at 35 °C. After 24 h, the obtained solution was kept under static conditions in a closed polypropylene bottle at 100 °C for 24 h. The white precipitate was filtered and dried at 100 °C until the solvent fully evaporated. The dried powder was calcined at 550 °C in air for 2 h.

2. Preparation of m-WO_3

The synthetic process is illustrated in Fig. 1(b). Using as-made KIT-6 as hard template, the WO_3 precursor (phosphotungstic acid hydrate, Sigma Aldrich) was impregnated into the pores of KIT-6 in ethanol while being evaporated. Phosphotungstic acid hydrate (1.8 g) and KIT-6 (0.45 g) were dissolved and dispersed in 20 mL of ethanol. The ethanol solvent was evaporated under slow stirring at room temperature. The dried powder was calcined at 550 °C in air for 2 h. Afterward, the WO_3/KIT-6 composite was etched with hydrofluoric acid (HF, Samchun Chemicals) overnight to remove the silica template, leaving the m-WO_3 replica of KIT-6.

3. Material Characterization

The morphologies of the prepared and commercial materials were characterized by field emission scanning electron microscopy (FE-SEM, Carl Zeiss SIGMA) and transmission electron microscopy (TEM, JEM-1011, JEOL, Ltd.). XRD patterns were obtained with a Bruker-AXS New D8-Advance diffractometer (Cu K_α radiation, wavelength=0.15406 nm). The Barrett-Joyner-Halenda (BJH) pore size distribution and Brunauer-Emmett-Teller (BET) surface area were investigated by N_2 adsorption measurements (Tristar II 3020, Micromeritics).

4. Electrochemical Characterization

The electrode was prepared by combining m-WO_3 or b-WO_3 (purchased from Daejung Chemicals and Metals), Super P, and polyvinylidene fluoride as active material, conductive agent, and binder in a ratio of 8 : 1 : 1, respectively. Using *N*-methyl-2-pyrrolidone (Sigma Aldrich) as solvent, the slurry was coated on Ti foil (~32 μm, Alfa Aesar). After drying under vacuum at 120 °C for 12 h, the electrode was punched to a diameter of 14 mm. Metallic Zn (Alfa Aesar) was used as both counter and reference electrode. A 2032 type coin cell was assembled using 3 m $Zn(CF_3SO_3)_2$ in DI water as electrolyte and glass fiber-A (GF/A) as separator.

Electrochemical analyses were performed with the as-prepared coin cell configuration. CV measurements were conducted in the voltage range of 0.1-0.9 V (*vs.* Zn/Zn^{2+}) at scan rates of 0.1, 0.2, 0.3, 0.5, 0.7, and 1.0 mV s^{-1}. The second cycle of each scan rate was plotted. Galvanostatic charge/discharge tests were also conducted with a current density of 50 mA g^{-1} in the same voltage range as the CV tests. Electrochemical impedance spectroscopy (EIS) was conducted with an amplitude of 10 mV in a frequency range from 0.1 Hz to 100 kHz. Rate performance test of m-WO_3 and b-WO_3 was at various current densities (0.01, 0.02, 0.03, 0.05, 0.1, and 0.01 A g^{-1}).

Ex situ XRD measurements were carried out in the first cycle after each cell reached certain potential values (discharging: 0.6, 0.1 V for m-WO_3 and 0.5, 0.1 V for b-WO_3; charging: 0.5, 0.9 V for both), using the constant/current constant voltage (CC/CV) method at a current density of 2 mA g^{-1}.

RESULTS AND DISCUSSION

1. Material Characterization

An impregnation method was employed to prepare m-WO_3 using KIT-6 as silica template. KIT-6 is a large mesoporous silica material possessing bicontinuous and interpenetrating channels with a 3D symmetric cubic network. After impregnation of the tungsten oxide precursor into the pores of KIT-6, followed by calcination and etching of the silica template with HF, we successfully obtained the tungsten oxide replica of KIT-6. Fig. 2 shows FE-

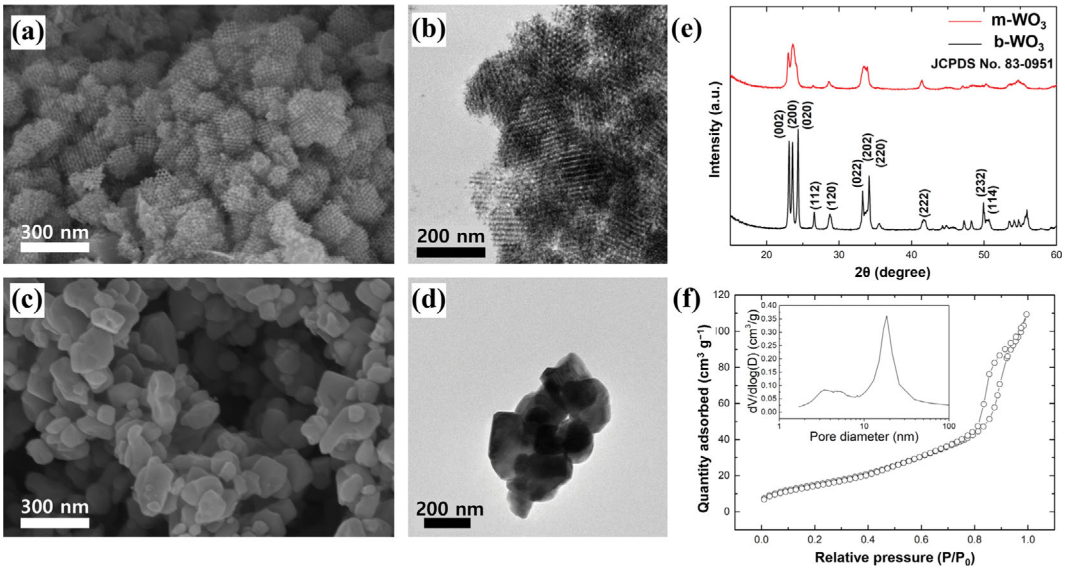

Fig. 2. SEM and TEM images of (a), (b) m-WO_3 and (c), (d) b-WO_3. (e) XRD patterns of m-WO_3 and b-WO_3. (f) N_2 adsorption-desorption curve of m-WO_3 and pore size distribution (PSD) calculated from the adsorption isotherm using the BJH method (inset).

SEM and TEM images of m-WO_3 and b-WO_3. As shown in the SEM images, compared with b-WO_3, m-WO_3 exhibited a highly ordered mesoporous structure, leading to a significant increase in surface area (Figs. 2(a) and 2(c)). The TEM images in Figs. 2(b) and 2(d) also confirm the mesoporous structure. In addition, the m-WO_3 and b-WO_3 had similar particle sizes (~100-150 nm), indicating that the effect of the particle size on the electrochemical performance was negligible. Fig. 2(e) displays the XRD patterns of m-WO_3 and b-WO_3. Both patterns were indexed to monoclinic WO_3 (JCPDS no. 83-0951), indicating no difference in crystalline phase between the two structures. However, they exhibited different crystallite sizes, as implied by the Debye-Scherrer equation:

$$D=K\lambda/\beta\cos\theta \qquad (1)$$

where D is the crystallite size, K is the Scherrer constant, λ is the X-ray wavelength, β is the full width at half maximum (FWHM) of the peak, and θ is the diffraction angle. According to the Debye-Scherrer equation, b-WO_3 had larger crystallite sizes corresponding to each peak compared to m-WO_3, as indicated by the narrower FWHM of the b-WO_3 patterns. The smaller grain sizes of m-WO_3 were attributed to the fact that the crystallite growth was restricted by the size of the pores of the KIT-6 template. Fig. 2(f) shows the nitrogen adsorption-desorption isotherms of m-WO_3. The nitrogen adsorption data show a mesoporous structure with pore sizes of ~20 and ~3.5 nm. The ~20 nm-sized pores were formed when the tungsten oxide precursor solution filled one of two bicontinuous chiral channels of KIT-6. The measured BET surface area and single point total pore volume were 50 m^2 g^{-1} and 0.17 cm^3 g^{-1}, respectively. In the case of b-WO_3, the BET surface area and single point total pore volume were 4 m^2 g^{-1} and 0.06 cm^3 g^{-1}, respectively. This successfully confirmed that the surface area of m-WO_3 was significantly higher than that of b-WO_3, due to the mesoporous structure. The higher surface area of m-WO_3 could lead to a higher specific capacitance because of its higher number of adsorption/desorption or redox reaction sites. In addition, the nanostructure of m-WO_3 resulted in a more stable cycling performance. This might be attributed to the fact that the mesoporous structure could effectively accommodate volume changes during cycling; moreover, the smaller crystallite sizes resulted in a weaker structural stress, leading to higher capacitance retention after long-term cycling. This will be discussed later in combination with Fig. 4(c).

2. Electrochemical Analysis

To evaluate the electrochemical properties of m-WO_3 and b-WO_3, we conducted CV tests within a voltage range of 0.1 to 0.9 V *vs.* Zn/Zn^{2+} (Fig. 3). Figs. 3(a) and 3(b) show the specific capacitance *vs.* voltage plots of m-WO_3 and b-WO_3, obtained by dividing the current density obtained from CV by the scan rate (at 0.1 mV s^{-1}). The m-WO_3 sample showed highly reversible redox reactions from the first cycle. At a scan rate of 0.1 mV s^{-1}, the two samples exhibited different peak positions, even though they had the same crystal structure. While cathodic and anodic peaks at ~0.4 and ~0.7 V (marked as red stars) were measured for b-WO_3, their counterparts for m-WO_3 were observed at ~0.5 and ~0.6 V, showing a smaller polarization. Moreover, the cathodic and anodic peaks of b-WO_3 ~0.6 and ~0.77 V (marked with blue triangles) became weaker after 30 cycles, while their counterparts for m-

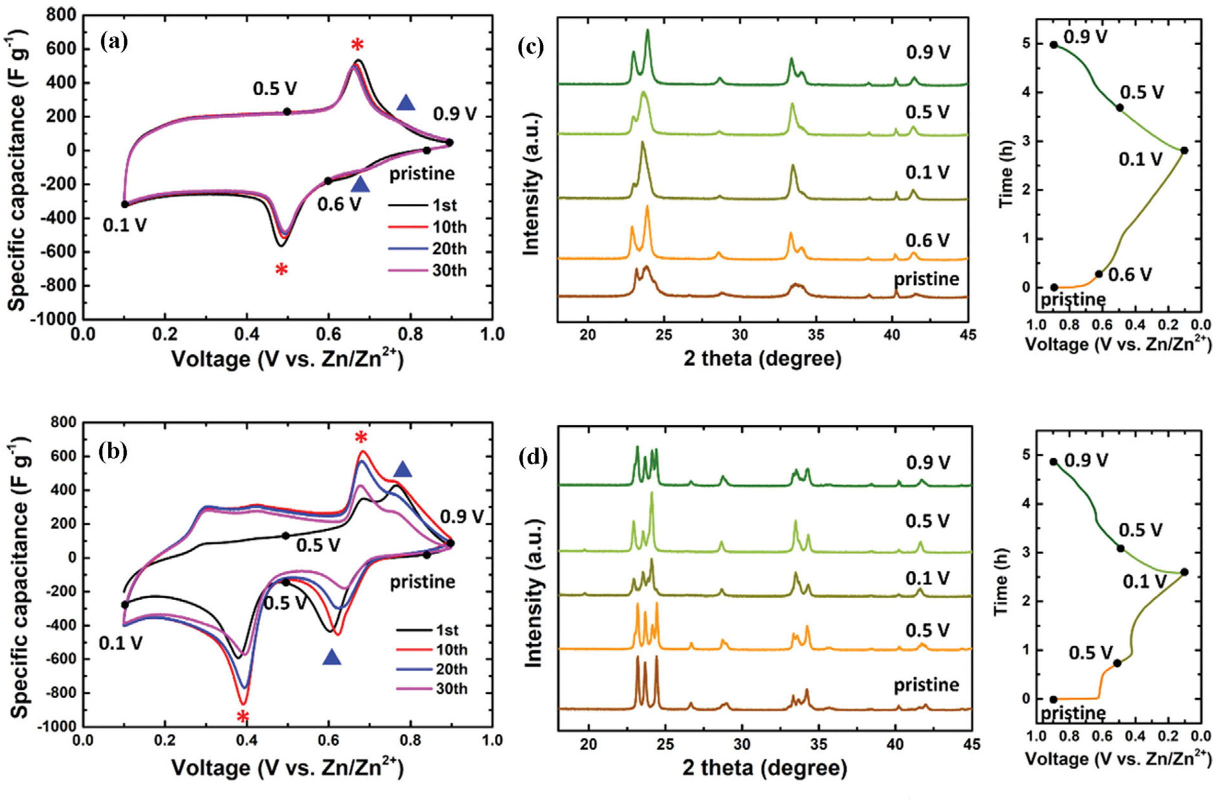

Fig. 3. Specific capacitance *vs.* voltage plots of (a) m-WO_3 and (b) b-WO_3 at a scan rate of 0.1 mV s^{-1}. *Ex situ* XRD patterns and voltage *vs.* time plots for the first cycle of (c) m-WO_3 and (d) b-WO_3.

WO_3 appeared as small peaks already from the first cycle. The fading of the peaks marked with blue triangles reflects the continuous structural degradation of b-WO_3, probably related to the specific capacitance decrease (Figs. 3(b) and 4(c)). In contrast, the small peak at the same potential (marked with blue triangles) of m-WO_3, which was largely maintained after cycling, showed the high reversibility of this sample. The most distinctive feature of a cyclic voltammogram is the shape. The CV curve of m-WO_3 exhibited a broader area compared to that of b-WO_3, similar to capacitor-type CV curves. The m-WO_3 sample underwent redox reactions in most voltage ranges, showing well-maintained shapes after cycling. In contrast, b-WO_3 exhibited a CV curve with clear redox peaks in specific voltage ranges and the curve shape changed after cycling. This result is consistent with previously reported results on the electrochemical behavior of nanostructured and bulk Nb_2O_5 [30]. Nanostructuring can also affect the crystal phase transitions during cycling. We investigated the changes in crystal structure during the first Zn^{2+} insertion/extraction using *ex situ* XRD measurements (Figs. 3(c) and 3(d)). Based on the CV curve of each sample, we selected the potentials after the redox peaks and observed the changes in the XRD patterns during discharging/charging, comparing the crystal phase at each point [31]. When discharged to 0.1 V, crystalline b-WO_3 existed as a mixture of monoclinic and tetragonal phases. After charging to 0.9 V, the crystal phase did not recover the pristine state, which implied that an irreversible phase transition occurred during the first cycle. This irreversible transition at the initial cycle was observed in the case of m-WO_3 as well. The only difference between the two samples was the shape of the XRD patterns. When discharged to 0.1 V, the crystal structure of m-WO_3 changed to the tetragonal phase. Considering that b-WO_3 showed a mixture of monoclinic and tetragonal phases after discharging to 0.1 V, m-WO_3 underwent a further phase transition. This result is consistent with a faster phase transition induced by the nanostructure, which will be discussed along with the GCD voltage profiles.

The electrochemical properties of m-WO_3 and b-WO_3 obtained *via* the GCD test are shown in Fig. 4. During the discharge process of b-WO_3, clear plateaus were observed at ~0.6 and ~0.4 V. (Fig. 4(b)). At these potentials, the crystal phase of b-WO_3 changed during Zn^{2+} insertion. Martínez-de la Cruz et al. observed the phase transition of WO_3 during Zn^{2+} insertion in an organic electrolyte system [12]. The two plateaus in the discharge curve were attributed to the two-phase reaction during Zn^{2+} insertion, in which the monoclinic phase changed to the tetragonal phase (~0.65 V) and then to the cubic phase (~0.4 V). On the other hand, the charge/discharge curve of m-WO_3 exhibited a linear shape compared to that of b-WO_3 (Fig. 4(a)). Dunn et al. explained that, when the particle size of the electrode material in a LIB system is smaller than a certain value, two phases cannot coexist because less Li^+ insertion is required for the phase transition, leading to a narrower curve plateau [32]. Similarly, the nanostructure of m-WO_3 prevents two phases from coexisting, because of the rapid phase transition during Zn^{2+} insertion leading to a linear discharge curve. Fig. 4(c) shows the cycling performance of m-WO_3 and b-WO_3. The specific capacitance of b-WO_3 was higher than that of m-WO_3 for the first 75 cycles. However, m-WO_3 exceeded the specific capacitance of b-WO_3 after the 75th cycle, showing a higher capacitance retention (~68%) after 200 cycles (the capacitance retention of b-WO_3 after 200 cycles was ~46%). We suggest probable reasons for the higher capacitance retention of m-WO_3: i) its mesoporous structure effectively accommodated volume changes during Zn^{2+} insertion/extraction; and ii) owing to its smaller crystallite sizes, m-WO_3 experienced weaker structural stress during the phase transition. Taking together the CV, *ex situ* XRD and GCD results (Figs. 3 and 4), m-WO_3 showed faster phase transitions from the initial cycle, with a high reversibility. Moreover, the well-preserved specific capacitance of m-WO_3 (Fig. 4(c)) is consistent with the reversibility presented in the CV curves (Figs. 3(a) and 3(b)). Electrochemical impedance spectroscopy (EIS) was conducted to see the resistance (Fig. S1). It shows the Nyquist plot of m-WO_3 and b-WO_3 after cycling. The semi-circle and straight line are related to the charge-transfer resistance (R_{ct}) and Warburg impedance, respectively. After cycling, there was no huge difference in the R_{ct} between m-WO_3 and b-WO_3 showing similar size of semi-circles. The total resistance of m-WO_3 (253 Ohm) was measured lower than that of b-WO_3 (346 Ohm). Rate performance was also measured at various current densities (Fig. S2). The decrease in specific capacitance of m-WO_3 at high current densities was smaller than that of b-WO_3, showing better rate performance. The better capacitance retention at high current density is attributed to the nanostructure of m-WO_3 with enlarged near-surface area and short-solid diffusion length, which led to fast intercalation of Zn^{2+} into the electrode materials.

To determine the effect of nanostructuring on the reaction mech-

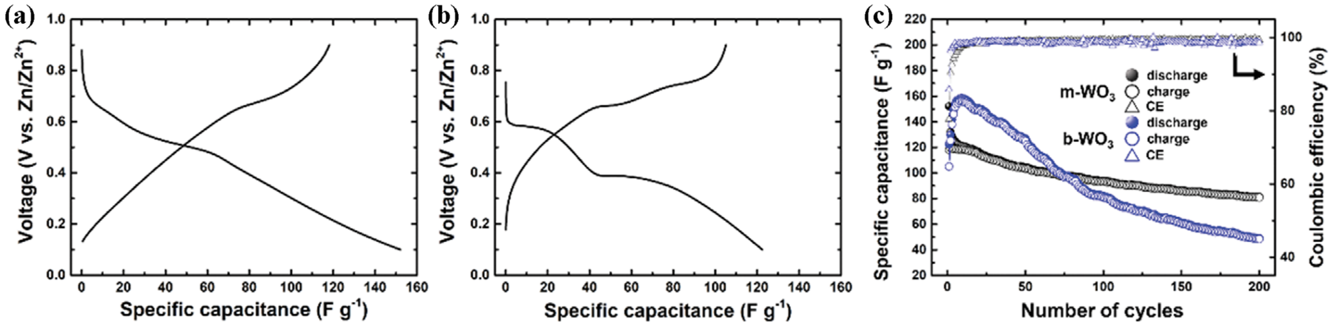

Fig. 4. Voltage profiles at the first cycle of (a) m-WO_3 and (b) b-WO_3 at a current density of 50 mA g^{-1}. (c) Cycling performance of m-WO_3 and b-WO_3 at a current density of 50 mA g^{-1} for 200 cycles.

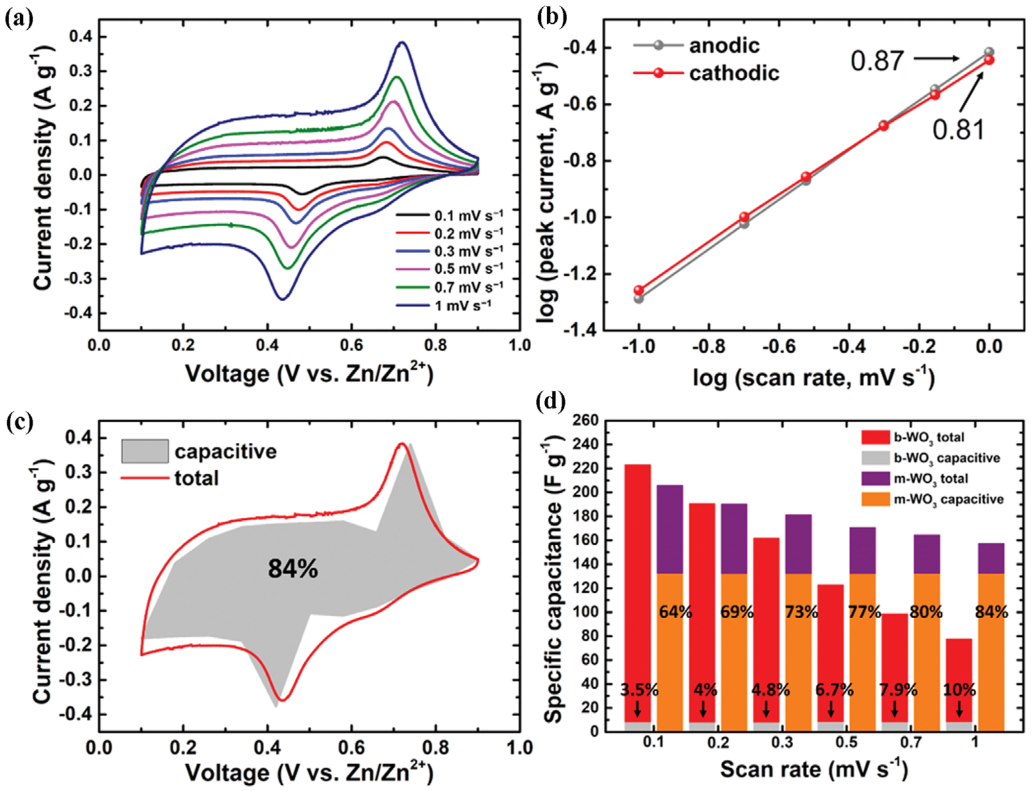

Fig. 5. (a), (b) CV curves and specific peak currents of m-WO$_3$ at various scan rates (0.1-1.0 mV s^{-1}). (c) CV curve of m-WO$_3$ at a scan rate of 1 mV s^{-1} showing total and capacitive currents. (d) Calculated specific capacitances and capacitive reaction contributions in b-WO$_3$ and m-WO$_3$ at various scan rates (0.1-1.0 mV s^{-1}).

anism, we quantified the contribution of diffusion-controlled and capacitive reactions *via* CV tests at various scan rates (0.1-1.0 mV s^{-1}) (Fig. 5) The relationship between peak current and scan rate can be expressed as $i=av^b$, where a and b are adjustable parameters. When the b value is 0.5, the reaction at the redox peak proceeds by a diffusion-controlled mechanism. In contrast, if the b value is 1, the process is controlled by a capacitive reaction. The measured b values at the cathodic and anodic peaks were 0.81 and 0.87, respectively (Fig. 5(b)). To quantify the contributions of the diffusion-controlled and capacitive reactions, the equation $i=av^b$ can be separated as $i=k_1v+k_2v^{1/2}$. When the latter is divided by $v^{1/2}$, k_1 and k_2 can be obtained as the slope and intercept of the resulting curve, whose values reflect the contributions of capacitive and diffusion-controlled reactions at certain voltages, respectively. As a result, the capacitive contribution in m-WO$_3$ was ~84% at 1 mV s^{-1} (Fig. 5(c)). The comparison with the capacitive reaction contribution, which was calculated to be only ~10% at the same scan rate, confirmed that the capacitive reaction become dominant upon nanostructuring, owing to the increased near-surface area and small-sized crystals (Fig. 5(d)). The effect of nanostructuring led to the higher contribution of capacitive reaction in m-WO$_3$, compared to that of bulk electrode. In addition, the mesoporous structure exhibited diverse crystalline structure during Zn^{2+} insertion/extraction (Fig. 3). These are likely due to the broad near-surface area and nanometer-sized crystallites in m-WO$_3$. Moreover, the well-preserved specific capacitance at higher scan rates in m-WO$_3$ also proves the fast and stable Zn^{2+}-intercalation (Fig. 5(d)). Throughout the results, we can confirm that the nanostructuring strategy facilitates crystal phase transition during (de)intercalation and provides capacitor-like behavior to active materials during charge/discharge.

CONCLUSION

We prepared m-WO$_3$ using a hard template method and investigated the effects of nanostructuring applied to an electrode material for aqueous Zn-ion systems. By measuring the *ex situ* XRD patterns of each charge/discharge state, we successfully confirmed the different phase transition behaviors of m-WO$_3$ and b-WO$_3$. Owing to its nanostructure, m-WO$_3$ underwent faster phase transition during Zn^{2+} insertion/extraction, with higher reversibility. The nanostructure of m-WO$_3$ also influenced the electrochemical behavior, showing better cycling performance and higher specific capacitance retention at high current conditions. The results of this study highlight the effects of nanostructuring and its promising potential as a strategy for enhancing the performance of electrode materials.

ACKNOWLEDGEMENTS

This research was supported by the Chung-Ang University Graduate Research Scholarship in 2021 and supported by National

Research Foundation of Korea (NRF) grant funded by the Korea government (2021M3D1A2043806 and 2021R1F1A1060230).

SUPPORTING INFORMATION

Additional information as noted in the text. This information is available via the Internet at http://www.springer.com/chemistry/journal/11814.

REFERENCES

1. Y. Qiu and F. Jiang, *Int. J. Heat Mass Transf.*, **184**, 122288 (2022).
2. R. Sebastian, *Process Saf. Prog.*, **41**, 426 (2022).
3. Y. Chen, Y. Kang, Y. Zhao, L. Wang, J. Liu, Y. Li, Z. Liang, X. He, X. Li, N. Tavajohi and B. Li, *J. Energy Chem.*, **59**, 83 (2021).
4. B. Tang, L. Shan, S. Liang and J. Zhou, *Energy Environ. Sci.*, **12**, 3288 (2019).
5. T. Xiong, Y. Zhang, W. S. V. Lee and J. Xue, *Adv. Energy Mater.*, **10**, 2001769 (2020).
6. S. Guo, L. Qin, T. Zhang, M. Zhou, J. Zhou, G. Fang and S. Liang, *Energy Stor. Mater.*, **34**, 545 (2021).
7. Z. Yi, G. Chen, F. Hou, L. Wang and J. Liang, *Adv. Energy Mater.*, **11**, 2003065 (2021).
8. Q. Yang, Q. Li, Z. Liu, D. Wang, Y. Guo, X. Li, Y. Tang, H. Li, B. Dong and C. Zhi, *Adv. Mater.*, **32**, 2001854 (2020).
9. T. Zhang, Y. Tang, S. Guo, X. Cao, A. Pan, G. Fang, J. Zhou and S. Liang, *Energy Environ. Sci.*, **13**, 4625 (2020).
10. T. Xiong, Y. Zhang, Y. Wang, W. S. V. Lee and J. Xue, *J. Mater. Chem. A*, **8**, 9006 (2020).
11. C. Jo, I. Hwang, J. Lee, C. W. Lee and S. Yoon, *J. Phys. Chem. C*, **115**, 11880 (2011).
12. A. Martínez-de la Cruz, L. M. Torres-Martínez, F. García-Alvarado, E. Morán and M. A. Alario-Franco, *J. Mater. Chem.*, **8**, 1805 (1998).
13. X. Xiao, T. Ding, L. Yuan, Y. Shen, Q. Zhong, X. Zhang, Y. Cao, B. Hu, T. Zhai, L. Gong, J. Chen, Y. Tong, J. Zhou and Z. L. Wang, *Adv. Energy Mater.*, **2**, 1328 (2012).
14. X. Chen, R. Huang, M. Ding, H. He, F. Wang and S. Yin, *ACS Appl. Mater. Interfaces*, **14**, 3961 (2022).
15. Y. Xia, T. Zhao, X. Zhu, Y. Zhao, H. He, C.-t. Hung, X. Zhang, Y. Chen, X. Tang, J. Wang, W. Li and D. Zhao, *Nat. Commun.*, **12**, 2973 (2021).
16. F. Schipper, H. Bouzaglo, M. Dixit, E. M. Erickson, T. Weigel, M. Talianker, J. Grinblat, L. Burstein, M. Schmidt, J. Lampert, C. Erk, B. Markovsky, D. T. Major and D. Aurbach, *Adv. Energy Mater.*, **8**, 1701682 (2018).
17. J. Cho, Y. J. Kim, T.-J. Kim and B. Park, *Angew. Chem. Int. Ed.*, **40**, 3367 (2001).
18. J. Meng, Q. He, L. Xu, X. Zhang, F. Liu, X. Wang, Q. Li, X. Xu, G. Zhang, C. Niu, Z. Xiao, Z. Liu, Z. Zhu, Y. Zhao and L. Mai, *Adv. Energy Mater.*, **9**, 1802695 (2019).
19. N. M. Trease, I. D. Seymour, M. D. Radin, H. Liu, H. Liu, S. Hy, N. Chernova, P. Parikh, A. Devaraj, K. M. Wiaderek, P. J. Chupas, K. W. Chapman, M. S. Whittingham, Y. S. Meng, A. Van der Van and C. P. Grey, *Chem. Mater.*, **28**, 8170 (2016).
20. D. Xu, B. Li, C. Wei, Y.-B. He, H. Du, X. Chu, X. Qin, Q.-H. Yang and F. Kang, *Electrochim. Acta*, **133**, 254 (2014).
21. H. Luo, B. Wang, F. Wu, J. Jian, K. Yang, F. Jin, B. Cong, Y. Ning, Y. Zhou, D. Wang, H. Liu and S. Dou, *Nano Energy*, **81**, 105601 (2021).
22. E. Lim, C. Jo, H. Kim, M.-H. Kim, Y. Mun, J. Chun, Y. Ye, J. Hwang, K.-S. Ha, K. C. Roh, K. Kang, S. Yoon and J. Lee, *ACS Nano*, **9**, 7497 (2015).
23. Q. Wang, Z. H. Wen and J. H. Li, *Adv. Funct. Mater.*, **16**, 2141 (2006).
24. H. Kim, M.-Y. Cho, M.-H. Kim, K.-Y. Park, H. Gwon, Y. Lee, K. C. Roh and K. Kang, *Adv. Energy Mater.*, **3**, 1500 (2013).
25. H.-G. Jung, N. Venugopal, B. Scrosati and Y.-K. Sun, *J. Power Sources*, **221**, 266 (2013).
26. X.-L. Wu, Y.-G. Guo, J. Su, J.-W. Xiong, Y.-L. Zhang and L.-J. Wan, *Adv. Energy Mater.*, **3**, 1155 (2013).
27. F. Kleitz, S. Hei Choi and R. Ryoo, *ChemComm*, 2136 (2003).
28. S. Yoon, E. Kang, J. K. Kim, C. W. Lee and J. Lee, *ChemComm*, **47**, 1021 (2011).
29. E. Kang, S. An, S. Yoon, J. K. Kim and J. Lee, *J. Mater. Chem.*, **20**, 7416 (2010).
30. M. Lübke, A. Sumboja, I. D. Johnson, D. J. L. Brett, P. R. Shearing, Z. Liu and J. A. Darr, *Electrochim. Acta*, **192**, 363 (2016).
31. M. Hočevar and U. Opara Krašovec, *Sol. Energy Mater. Sol. Cells.*, **154**, 57 (2016).
32. J. Wang, J. Polleux, J. Lim and B. Dunn, *J. Phys. Chem. C*, **111**, 14925 (2007).

Supporting Information

Pseudocapacitive behavior of mesoporous tungsten oxide in aqueous Zn^{2+} electrolyte

Woosuk Kang*, **Inho Nam*,**,†**, **and Changshin Jo***,****,†**

*School of Chemical Engineering & Materials Science, Chung-Ang University (CAU),
84 Heukseok-ro, Dongjak-gu, Seoul 06974, Korea
**Department of Intelligent Energy and Industry, Department of Advanced Materials Engineering,
Chung-Ang University (CAU), 84 Heukseok-ro, Dongjak-gu, Seoul 06974, Korea
***Graduate Institute of Ferrous & Energy Materials Technology (GIFT), Pohang University of Science and Technology
(POSTECH), 77 Cheongam-ro, Nam-gu, Pohang, Gyeongbuk 37673, Korea
****Chemical Engineering, Pohang University of Science and Technology (POSTECH),
77 Cheongam-ro, Nam-gu, Pohang, Gyeongbuk 37673, Korea

(*Received 15 September 2022* • *Revised 6 December 2022* • *Accepted 8 December 2022*)

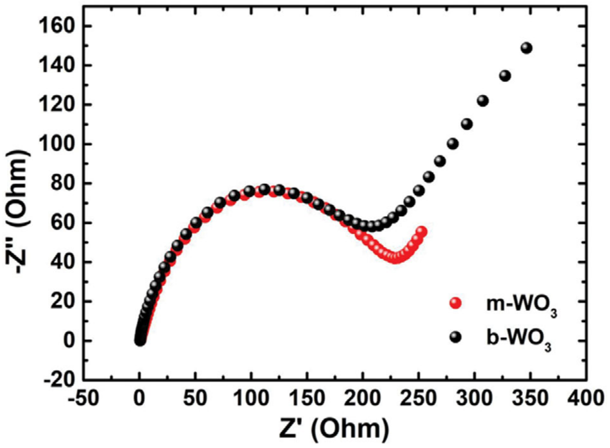

Fig. S1. Nyquist plots of m-WO_3 and b-WO_3 after cycled.

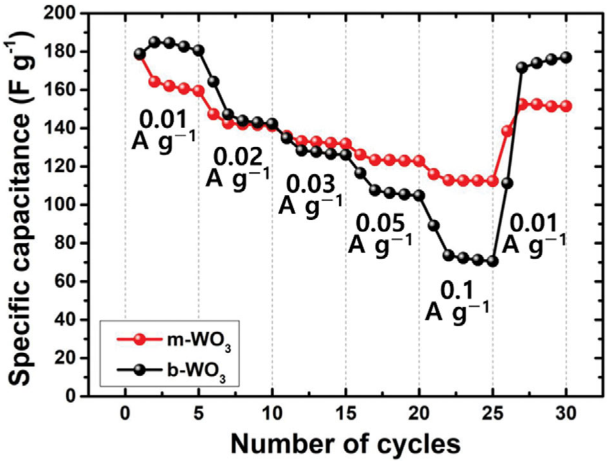

Fig. S2. Rate performance of m-WO_3 and b-WO_3 at various current densities (0.01, 0.02, 0.03, 0.05, 0.1, and 0.01 A g^{-1}, 5 cycles for each current density).